nature
materials

Electrodes on the brain

OXIDE ELECTRONICS
All records beaten

LIGHT-EMITTING TRANSISTORS
Layers for light

CARBON NANOTUBES
Sugar-coated radiotherapy

1. REPORT DATE **18 APR 2010**	2. REPORT TYPE	3. DATES COVERED **00-00-2010 to 00-00-2010**

4. TITLE AND SUBTITLE	5a. CONTRACT NUMBER
Dissolvable films of silk fibroin for ultrathin conformal bio-integrated electronics	5b. GRANT NUMBER
	5c. PROGRAM ELEMENT NUMBER

6. AUTHOR(S)	5d. PROJECT NUMBER
	5e. TASK NUMBER
	5f. WORK UNIT NUMBER

7. PERFORMING ORGANIZATION NAME(S) AND ADDRESS(ES) **University of Illinois at Urbana-Champaign,Department of Materials Science and Engineering,Beckman Institute for Advanced Science and Technology,Urbana,IL,61801**	8. PERFORMING ORGANIZATION REPORT NUMBER

9. SPONSORING/MONITORING AGENCY NAME(S) AND ADDRESS(ES)	10. SPONSOR/MONITOR'S ACRONYM(S)
	11. SPONSOR/MONITOR'S REPORT NUMBER(S)

12. DISTRIBUTION/AVAILABILITY STATEMENT **Approved for public release; distribution unlimited**

13. SUPPLEMENTARY NOTES

14. ABSTRACT

15. SUBJECT TERMS

16. SECURITY CLASSIFICATION OF:			17. LIMITATION OF ABSTRACT	18. NUMBER OF PAGES	19a. NAME OF RESPONSIBLE PERSON
a. REPORT **unclassified**	b. ABSTRACT **unclassified**	c. THIS PAGE **unclassified**	**Same as Report (SAR)**	**27**	

Dissolvable films of silk fibroin for ultrathin conformal bio-integrated electronics

Dae-Hyeong Kim and Jonathan Viventi *et al.*[*]

Electronics that are capable of intimate, non-invasive integration with the soft, curvilinear surfaces of biological tissues offer important opportunities for diagnosing and treating disease and for improving brain/machine interfaces. This article describes a material strategy for a type of bio-interfaced system that relies on ultrathin electronics supported by bioresorbable substrates of silk fibroin. Mounting such devices on tissue and then allowing the silk to dissolve and resorb initiates a spontaneous, conformal wrapping process driven by capillary forces at the biotic/abiotic interface. Specialized mesh designs and ultrathin forms for the electronics ensure minimal stresses on the tissue and highly conformal coverage, even for complex curvilinear surfaces, as confirmed by experimental and theoretical studies. *In vivo*, neural mapping experiments on feline animal models illustrate one mode of use for this class of technology. These concepts provide new capabilities for implantable and surgical devices.

Strategies for bio-integrated electronics must overcome challenges associated with the mismatch between the hard, planar surfaces of semiconductor wafers and the soft, curvilinear tissues of biological systems. These differences in mechanics and form lead, almost invariably, to low-fidelity coupling at the biotic/abiotic interface and limited long-term tissue health. The difficulties are most pronounced, and the solutions are perhaps most important, in systems designed for brain/computer interfaces (BCIs). State-of-the-art penetrating microelectrode arrays consist of sharp shanks, typically 10×10 arrays of pins with base widths $\sim 80\,\mu m$, lengths $\sim 1.5\,mm$ and pitch $\sim 400\,\mu m$ (ref. 1). These arrays are rigid and inflexible because of their construction from blocks of silicon, which also supports their conventional wafer-based electronics. They are valuable for research in BCIs, but they damage tissue and do not offer long-term electrical interface stability[2] because of unwanted biological responses to the electrodes. Comparable BCI performance can be achieved with non-penetrating, surface electrode systems that are minimally invasive and provide greatly improved stability[3–5] with minimized inflammation. Standard clinical subdural electrode arrays are useful for BCIs (ref. 6) but their widely spaced ($\sim 1\,cm$), large contact electrodes ($\sim 0.35\,cm$ diameter) spatially undersample the electrical signals present on the surface of the brain[7]. Decreasing the spacing and size of the measurement points can improve BCI performance by providing access to high temporal and spatial frequency signals[8]. Such designs, however, demand excellent conformal coverage over the highly convoluted brain surface, to ensure direct coupling between brain tissue and the electrodes.

Reducing the thickness of the substrate decreases the bending rigidity, thereby improving conformal contact. Unfortunately, clinical arrays and even the thinnest devices designed for research have thicknesses ($700\,\mu m$ and $>10\,\mu m$ (refs 9,10), respectively) that are larger than desired to ensure conformal contact. Analogous systems based on stretchable substrates have also been explored in other neural interfaces[11,12] but typically with similar or larger thicknesses. In conventional designs, ultrathin geometries (that is, $<10\,\mu m$) are impractical, because the films are not sufficiently self-supporting to be manipulated effectively during fabrication or implantation.

Silk is an appealing biopolymer as a temporary, soluble supporting substrate for this application because it is optically transparent[13,14], mechanically robust and flexible in thin-film form[15–17], compatible with aqueous processing[18,19] and amenable to chemical and biological functionalization[13,20]. The silk, in both the non-treated and methanol-treated formats, is biocompatible[21,22], bioresorbable[23] and water soluble with programmable rates of dissolution[15,16]. Moreover, recent work demonstrates the ability of silk films to serve as a platform for transistors[23] and various classes of photonic devices[24,25]. The process of preparing silk substrates for the purposes reported here began with material derived from *Bombyx mori* cocoons, and followed published procedures[18,19]. Briefly, boiling the cocoons in a $0.02\,M$ aqueous solution of sodium carbonate for $60\,min$ removed sericin, a water-soluble glycoprotein that binds fibroin filaments in the cocoon but can induce undesirable immunological responses[21,26]. An aqueous solution of lithium bromide at $60\,^{\circ}C$ solubilized the fibres and subsequent dialysis removed the lithium bromide. Centrifugation followed by micro filtration eliminated particulates to yield solutions of 8–10% silk fibroin with minimal contaminants. Casting a small amount of the solution on a flat piece of poly(dimethylsiloxane) (PDMS) followed by crystallization in air ($\sim 12\,h$) yielded uniform films (thickness of 20–50\,\mu m) (Fig. 1a) that were subsequently removed from the PDMS for integration with separately fabricated electronics.

For the systems described in the following, ultrathin, spin-cast films of polyimide (PI) served as a support for arrays of electrodes designed for passive neural recording. Control devices consisted of otherwise similar layouts, but formed using standard photolithographic procedures applied directly on commercial PI sheets with thicknesses of 25 and $75\,\mu m$ (Supplementary Fig. S1). Anisotropic conductive film (ACF) bonded to electrode pads at one end of the arrays provided electrical connection to external data acquisition systems (Supplementary Fig. S2). Ultrathin PI films, with or without mesh layouts, cannot be manipulated effectively for processing, interconnecting or implanting onto the brain because of their extreme flexibility and mechanical fragility. For these cases, the fabrication process exploited layers of PI spin-cast onto silicon wafers coated with sacrificial films of

---

[*]A full list of authors and their affiliations appears at the end of the paper.

511
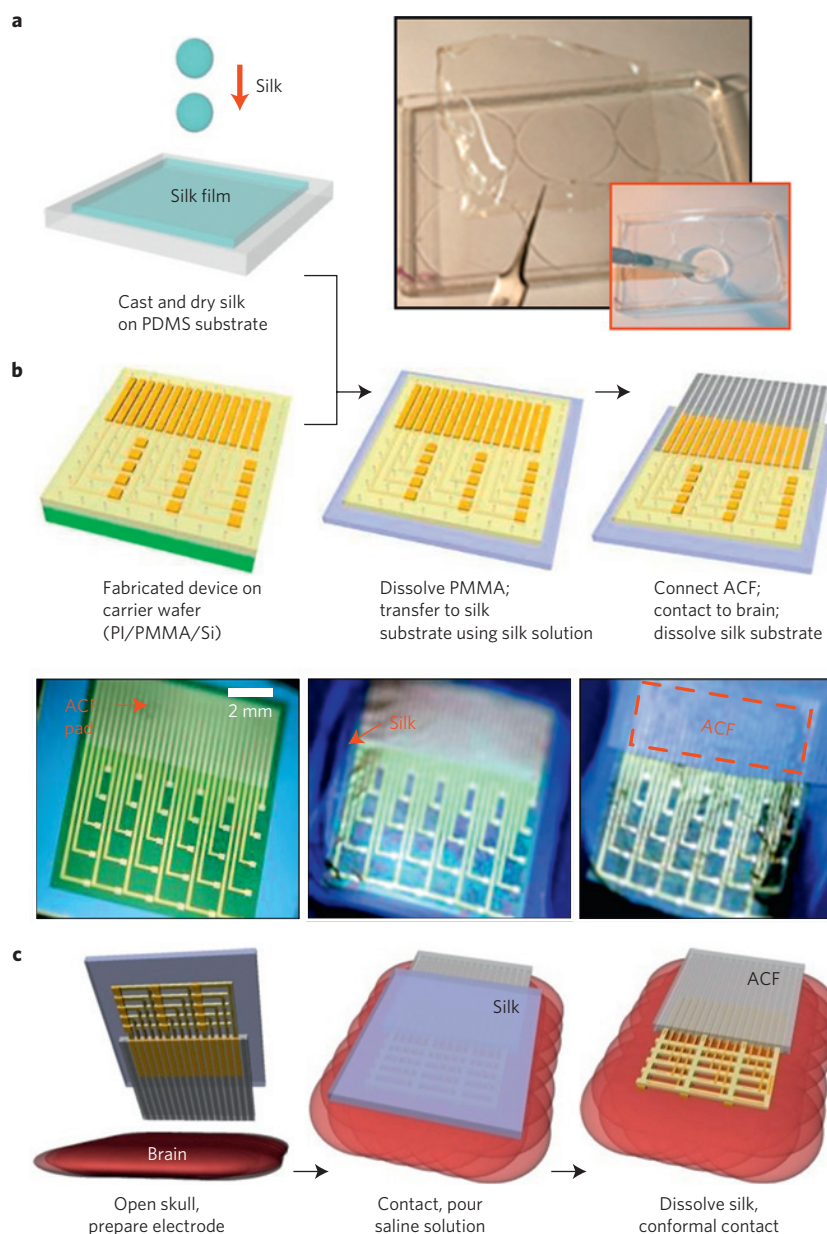
Figure 1 | Schematic illustration and images corresponding to steps for fabricating conformal silk-supported PI electrode arrays. a, Casting and drying of silk fibroin solution on a temporary substrate of PDMS; 5–15-μm-thick silk film after drying for 12 h at room temperature. **b**, Steps for fabricating the electrode arrays, transfer printing them onto silk and connecting to ACF cable. **c**, Schematic illustration of clinical use of a representative device in an ultrathin mesh geometry with a dissolvable silk support.

poly(methylmethacrylate) (PMMA) (left frame of Fig. 1b). After electrode fabrication, the mesh structure devices underwent further etching to remove unwanted parts of the PI. The processing was completed by dissolving the PMMA layer with acetone, transfer printing the entire assembly to a film of silk and connecting the ACF, yielding easily manipulated bioresorbable neural recording systems. See schematic illustrations and images in Fig. 1b. In all cases, the arrays consisted of 30 measurement electrodes (Au, 150 nm) in a 6 × 5 configuration, each with dimensions of 500 μm × 500 μm and spaced by 2 mm. Interconnection wires were protected by a thin (∼1.2 μm) overcoat of PI to prevent contact with the tissue or surrounding fluids. Choosing the thickness of the PI passivation layer to match that of the PI substrate locates the interconnects at the neutral mechanical plane, thereby minimizing the potential for bending-induced mechanical fracture. Details of the fabrication steps appear in the Methods

section. Electrode arrays were implanted by placing them on the exposed brain (after craniotomy) and then flushing with saline to dissolve the silk. This procedure induced spontaneous, conformal wrapping of the device, as illustrated schematically for the mesh design in Fig. 1c. After the measurements, the electrode array can be easily removed, because of the attachment of the electrodes to the ACF.

The sequence of images in Fig. 2a shows the dissolution process for a representative case (7-μm-thick PI film, connected to ACF on a silk substrate with a thickness of ∼25 μm) inserted into warm water (∼35 °C). As the silk substrate disappears, the total bending stiffness, EI, diminishes markedly because of its cubic dependence on thickness. Computed results appear in Fig. 2b and Supplementary Fig. S3c for PI thicknesses of 2.5 and 7 μm. To highlight the benefits of reduced thickness, the inset shows the ratio of EI for these two cases. Through programmed control
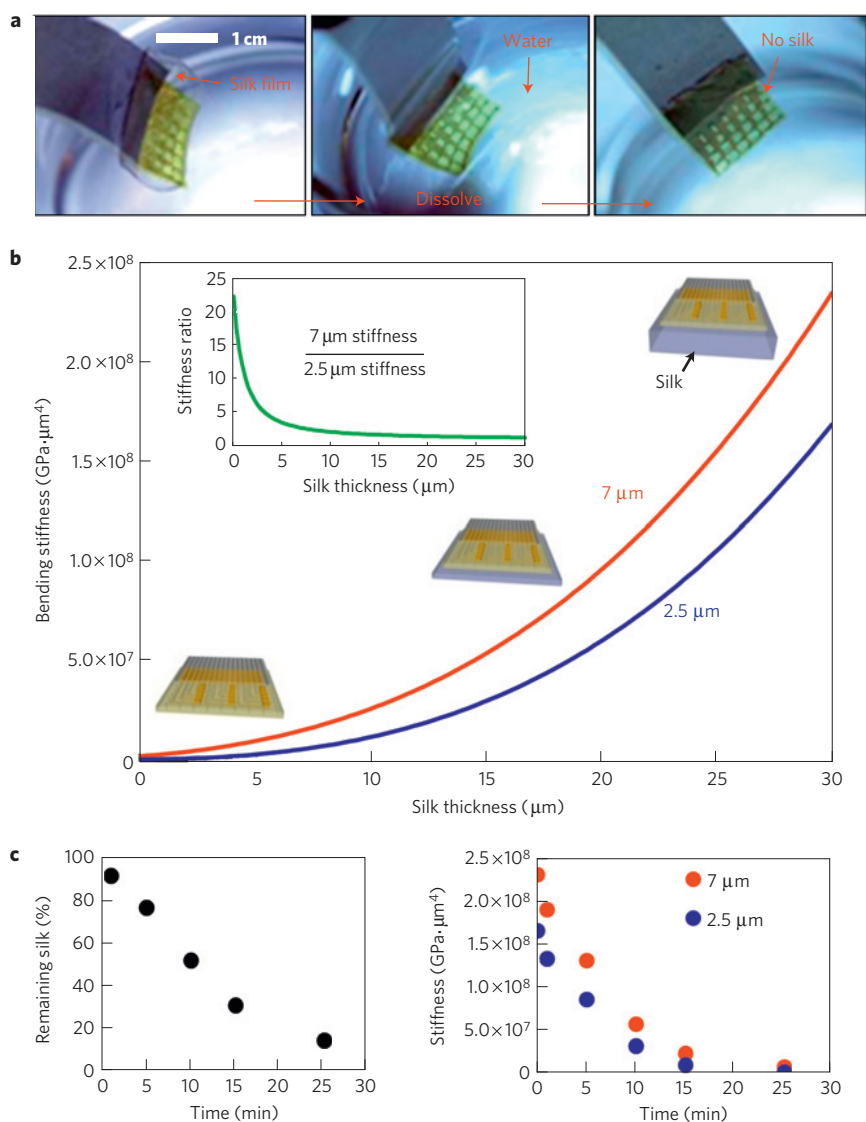
Figure 2 | Time-dependent changes as the silk substrate dissolves. a, Dissolution of the silk through submersion in warm water. **b**, Total bending stiffness of 7 μm and 2.5 μm electrode arrays on supporting silk films as a function of the thickness of the supporting silk film. Inset: The ratio of bending stiffness between 7 μm and 2.5 μm. **c**, Time-dependent change in the volume of a silk film during dissolution (left frame) and bending stiffness calculated for silk treated in 70% ethanol for 5 s for two different array thicknesses (right frame). The 5 s ethanol treatment increases the dissolution time from minutes to about 1 h.

of the dissolution rate by modifications of the silk protein secondary structure[15,16], these changes in EI can be designed to occur over periods of time ranging from seconds to years, depending on requirements. Figure 2c shows, as an example, the dissolution rate of silk film slightly treated with ethanol (left frame) and the computed time dependence of EI in devices that employ more thorough ethanol treatment (right frame). The error range for silk thickness measurement is ±7%. See Supplementary Information for detailed conditions. This dissolution time can be lengthened even more by extending the treatment time to days or weeks[15]; the corresponding time dependence of EI appears in Supplementary Fig. S4.

To examine the ability of these systems to conform to relevant surfaces, we carried out experiments using a human brain model, following the basic steps shown in Fig. 1c. Figure 3 provides images for various cases after washing with saline, including relatively thick control devices that do not incorporate silk. Clearly, the extent of conformal coverage increases with decreasing thickness; the mesh design provides further improvements, as shown in Fig. 3d,

Supplementary Figs S5 and S6. To reveal the underlying mechanics, we carried out systematic and quantitative studies on well-defined surfaces that capture certain basic features of the curvature of the brain. The first set of experiments explored wrapping the devices on isolated and overlapped cylindrical surfaces. Figure 4a shows the simplest case of a device with bending stiffness EI, thickness h, width b and length $2L$, wrapped on a cylinder with radius R. Analytical expressions for EI can be written for the multilayer structures of Fig. 1 in terms of materials properties and geometries, as described in the Supplementary Information. For the wrapped state to be energetically favourable,

$$\gamma \geq \gamma_c = \frac{EI}{2R^2 b} \quad (1)$$

where γ is the adhesion energy per unit area. The bottom frame of Fig. 4a compares the above relation with a series of experiments (Supplementary Fig. S7). The data, the error range of which is ±5%, are consistent with $\gamma \sim 10\ \mathrm{mJ\,m^{-2}}$, which is comparable to
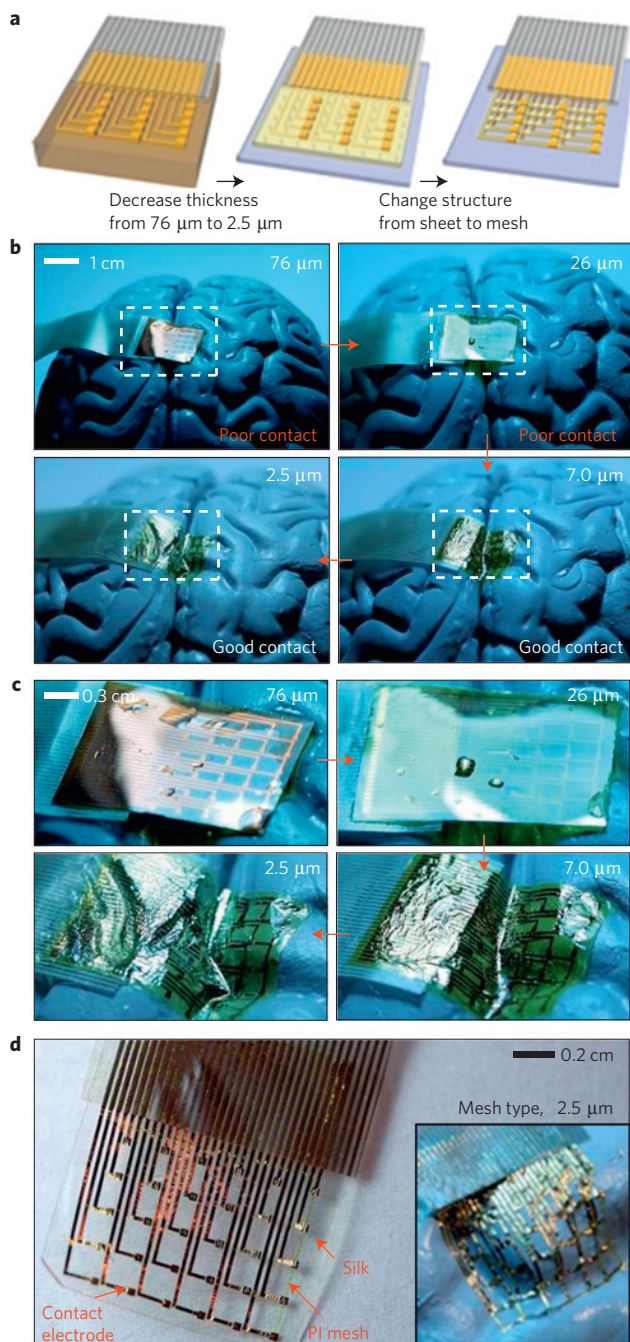
Figure 3 | Neural electrode arrays of varying thickness on simulated brain models to illustrate flexibility. a, Schematic illustration of trends in thickness and structure that improve conformal contact. **b**, Series of pictures illustrating how the thickness of the electrode array contributes to conformal contact on a brain model. **c**, Magnified view of the pictures in **b**. **d**, Image of an electrode array with a mesh design on a dissolvable silk substrate. The arrows indicate struts in the mesh that help to stabilize the Au interconnects after dissolution of the silk. The inset illustrates the high degree of conformal contact that can be achieved on the brain model once the silk substrate has been dissolved.

reported values for wet interfaces[27]. Reducing the thickness provides clear benefits, for example, wrapping cylinders using only capillary adhesion forces is possible for $R \sim 1$ cm when $h < \sim 15\,\mu m$.

A pair of overlapped cylinders represents a simple model for a gyrus of the brain. Figure 4b shows cylinders with radii R, a centre-to-centre separation of $2d$ and connected by a smooth arc of

radius r_0, at the angular position $\theta_0 = \sin^{-1}[d/(R+r_0)]$. The contact angle of a thin film with one cylinder, θ, can be shown to be

$$\frac{R\sin\theta}{d - R\sin\theta} + \frac{dR\theta\cos\theta}{(d - R\sin\theta)^2} - \left(\frac{\gamma}{\gamma_c} - 1\right)\left(1 - \frac{d}{R\sin\theta} + \frac{d\theta\cos\theta}{R\sin^2\theta}\right) = 0 \quad (2)$$

where γ_c is given in equation (1). The solution of equation (2) takes the form $\theta = \theta(d/R, \gamma/\gamma_c)$. For $\gamma < \gamma_c$, the energy has a minimum at $\theta = 0$, and the film does not wrap around the cylinders. Partial wrapping occurs to a contact angle of θ (that is, contact for angles between 0 and $\theta < \theta_0$) for $\gamma_c \leq \gamma < \gamma_c'$, where γ_c' is obtained from equation (2) with $\theta = \theta_0$ as given in the Supplementary Information. For $\gamma \geq \gamma_c'$, wrapping is complete (that is, conformal contact for angles between 0 and θ_0). By comparing equation (2) with the experiment in Supplementary Fig. S8, the extracted adhesion energy per unit area is $\gamma = 10\,mJ\,m^{-2}$. Results appear in the bottom frame of Fig. 4b, where the parameters correspond roughly to features on the brain model: $R = 6.14$ mm, $d = 5.93$ mm and $r_0 = 1.72$ mm. The error range of the data is $\pm 5\%$. (Experimental images appear in Supplementary Fig. S8.) By substituting θ with θ_0 in equation (2), the critical thickness for conformal contact is obtained as $h_0 = 4.9\,\mu m$ for the present system; that is, devices thinner than $\sim 4.9\,\mu m$ achieve conformal contact on this surface. The experimental results are consistent with this calculation.

Cylindrical surfaces such as those of Fig. 4a,b are developable; the brain is not. As a model non-developable surface, we examined the case of a hemispherical substrate. Figure 4c shows results for electrode arrays with sheet designs at thicknesses of 7 and 2.5 μm and with an open mesh layout[28] at 2.5 μm, each on a glass hemisphere with a radius of curvature of 6.3 mm. With only water capillarity as the adhesion force, the mesh electrode array achieves excellent conformal contact. The sheets show comparatively poor contact, with large wrinkles, even for the thinnest case (that is, 2.5 μm). Mechanical analysis of a simple model reveals the underlying physics. The left frame of Fig. 4d shows the mechanics model for the sheet design, which consists of a circular film with radius $r + w$ wrapped onto a sphere with radius R. The central green part denotes a PI plate of radius r, tension stiffness $(Eh)_{PI}$ and equi-biaxial bending stiffness $(EI)_{PI}$. The yellow ring corresponds to a multilayer structure of PI and Au, of width w, tension stiffness $(Eh)_{composite}$ and equi-biaxial bending stiffness $(EI)_{composite}$. For the film to wrap around the sphere, the required minimum adhesion energy per unit area is obtained analytically as

$$\gamma_c^{sheet} = \frac{(EI)_{PI}}{R^2} + \frac{(Eh)_{PI}}{r^2}\int_0^r \left(1 - \frac{R}{x}\sin\frac{x}{R}\right)^2 x\,dx$$

$$+ \frac{2w(EI)_{composite}}{rR^2} + \frac{w(Eh)_{composite}}{r}\left(1 - \frac{R}{r}\sin\frac{r}{R}\right)^2 \quad (3)$$

A mechanics model for the mesh design appears in the right frame of Fig. 4d, which consists of only a circular strip of a corresponding multilayer of PI and Au. In this case, the minimum adhesion energy per unit area is

$$\gamma_c^{mesh} = \frac{(EI)_{composite}}{R^2} + \frac{w^2(Eh)_{composite}}{24r^2}\left(1 - \sqrt{1 - \frac{r^2}{R^2}}\right)^2 \quad (4)$$

For the case that $w \ll r$, γ_c^{sheet} in equation (3) is always larger than γ_c^{mesh} in equation (4); that is, $\gamma_c^{sheet} > \gamma_c^{mesh}$. The inference is that the open mesh design requires a much lower adhesion energy than the corresponding sheet, thereby leading to greatly improved ability for conformal coverage, as shown in Supplementary Fig. S9a. Supplementary Fig. S9c shows critical adhesion energies for films with thicknesses up to 80 μm. For a thickness of 2.5 μm and

$w/r = 4$, $\gamma_c^{sheet} = 29.1\,\mathrm{mJ\,m^{-2}}$ for the sheet, which is more than 12 times larger than the mesh $\gamma_c^{mesh} = 2.4\,\mathrm{mJ\,m^{-2}}$. In addition, the mesh design involves membrane strains that are smaller, by roughly a factor of w/r, compared with sheets with similar thickness. For the experimental mesh systems, this ratio is of the order of 1/4. As a result, for a representative critical wrinkling strain of 0.1%, nearly two thirds of the sheet will wrinkle. Under the same conditions, the entire mesh gives perfect, conformal contact. Finally, the normal (peeling) interfacial stress for the mesh is only 1/4 of that for the sheet (Supplementary Figs S9b and S9d), leading to improved adhesion and reduced forces applied to the substrate. See Supplementary Information for details.

In vivo neural monitoring experiments on a feline animal model demonstrated the practical implications of these favourable mechanics. The tests involved an anaesthetized cat with its head fixed in a stereotaxic apparatus and its eyes focused on a monitor that subtended $28° \times 22°$ of space. An initial craniotomy and durotomy exposed a $2 \times 3\,\mathrm{cm}$ region of cortex. The electrode arrays covered much of the visual cortex as shown in the left frames of Fig. 5a–c. Visual stimuli consisted of full-field drifting gratings presented for 1 s at 2 Hz with a spatial frequency of 0.5 cycles per degree. Gratings were presented at two different directions over eight different orientations (16 unique stimuli). However, the responses obtained from all 16 unique stimuli were averaged to obtain the largest possible signal-to-noise ratio.

Three kinds of electrode array were used for comparison: 76-μm- and 2.5-μm-thick sheets and a 2.5 μm-thick mesh. The second two included dissolvable silk supports. The left images of Fig. 5a–c illustrate the progressively improved conformal contact with reduced thickness (that is, 76 μm to 2.5 μm, in Fig. 5a and b, respectively) and with introduction of the mesh (that is, Fig. 5c). The right frames of Fig. 5a–c demonstrate the effectiveness of decreasing the electrode thickness and the mesh structure on physiological measurements of brain activity.

In particular, these frames show the average evoked response measured at each electrode, each plotted in a spatial arrangement that corresponds to the images in the left frames. Prominent visually evoked potentials are observed, particularly a strong P100 response. The P100 response is a 'positive' evoked response typically occurring at 100 ms after the stimulation onset[29]. The P100 responses shown in Fig. 5 are plotted positive down, by convention. The background colour of each plot illustrates a quantitative measure of the evoked response signal quality. This measure of signal quality was calculated by dividing the root mean square (rms) amplitude of each average electrode response in the 200 ms window immediately after the presentation of the visual stimulus by the rms amplitude of the average 1.5 s window immediately preceding the stimulus presentation. The colour bar at the bottom of Fig. 5c provides the numerical scale for all of the colours used in Fig. 5a–c. This measurement serves as a quantitative metric of the electrode performance, because the uniform nature of the stimulation is expected to evoke similar responses across the entire visual cortex.

In each case, 28 of the 30 electrode channels were recorded and evaluated for evoked potential response, as coloured in green to red. Two channels, indicated in grey, were reserved as local references, as required by the recording apparatus, and were not evaluated. The channels with high and low rms amplitude ratios are coloured green and red, respectively. The 76 μm (Fig. 5a) electrode array exhibited the lowest performance with a mean rms amplitude ratio of all 28 channels of 3.6 ± 1.8. This was due to poor contact at many of the electrodes. The 2.5 μm array (Fig. 5b) showed better conformal contact and correspondingly a higher mean rms amplitude ratio of 5.2 ± 3.9. However, the higher standard deviation and correspondingly wide spectrum of the red and green channels on the array indicate that although many electrodes recorded excellent signals, approximately half of the electrodes still had poor contact
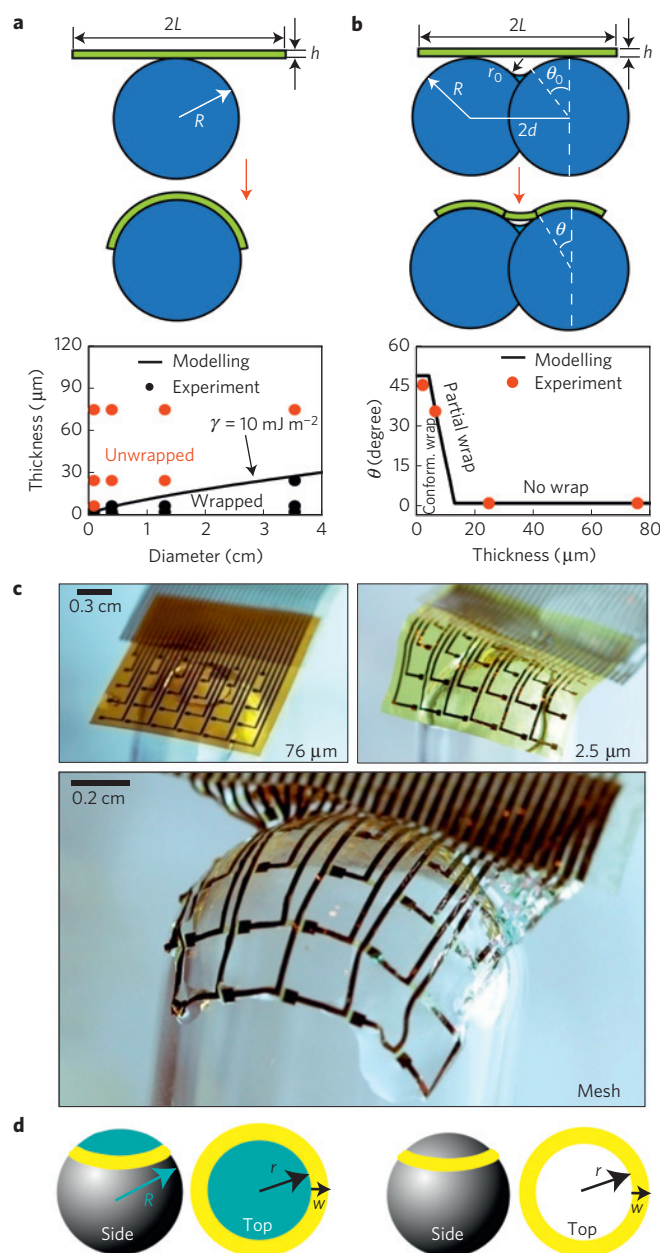
Figure 4 | Mechanical modelling, theoretical predictions and measured properties. a, A thin film wrapped around a cylinder of radius *R*. The unwrapped and wrapped states appear in the top and centre frames, respectively. The bottom frame compares the mechanics model and experiments. **b**, A thin film wrapped around two overlapped cylinders. The top and centre frames show the unwrapped and wrapped states, respectively. The bottom frame shows a comparison between the mechanics model and experiments. **c**, Images of electrode arrays (76 μm sheet in left top, 2.5 μm sheet in right top and 2.5 μm mesh in bottom panel) wrapped onto a glass hemisphere. **d**, Mechanics models for sheet (left frame) and mesh (right frame) designs.

with the brain and recorded weak responses. The 2.5 μm mesh electrode (Fig. 5c) showed the best performance, with nearly all channels in good contact and a still higher mean rms amplitude ratio of 5.7 ± 3.0. The lower standard deviation of the 2.5 μm array illustrates that most of the electrodes recorded good responses.

Figure 5d shows representative single-channel data from one of the 2.5 μm mesh electrodes. A sleep spindle is observed with good signal amplitude and signal-to-noise ratio. This collective set of
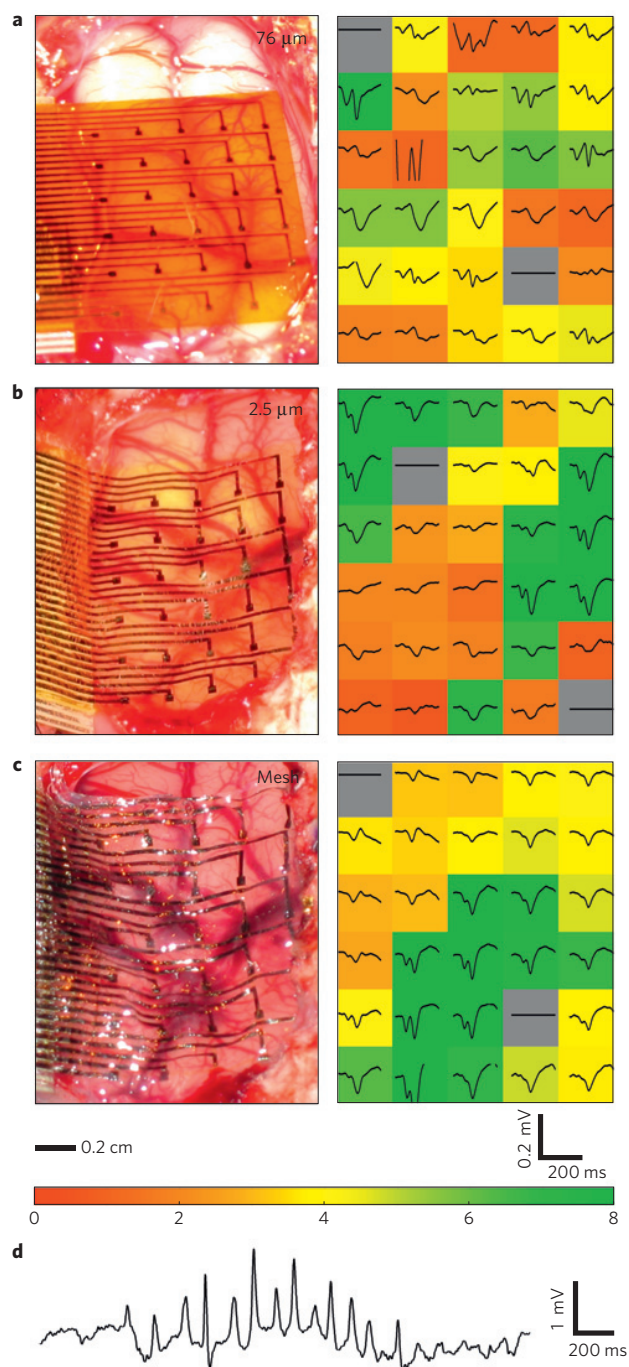
Figure 5 | Photographs and data from animal validation experiments.
a–c, Image of an electrode array on a feline brain (left) and the average evoked response from each electrode (right) with the colour showing the ratio of the rms amplitude of each average electrode response in the 200 ms window (plotted) immediately after the presentation of the visual stimulus to the rms amplitude of the average 1.5 s window (not shown) immediately preceding the stimulus presentation for a 76 µm (**a**), 2.5 µm (**b**) and 2.5 µm mesh (**c**) electrode array. The stimulus presentation occurs at the left edge of the plotted window. In all three images, the occipital pole is at the bottom of the frame and the medial is at the right. The scale bars at the bottom of **c** indicate the spatial scale for the left frames and the voltage and timescales for the right frames of **a–c**. The colour bar at the bottom of **c** provides the scale used in the right frames of **a–c** to indicate the rms amplitude ratios. **d**, Representative voltage data from a single electrode in a 2.5 µm mesh electrode array showing a sleep spindle.

observations is consistent with the systematic mechanics studies described previously. We did not observe any evidence of immune response. Histology data from related types of device implanted under the skin exhibited no inflammation after 4 weeks, as shown in Supplementary Fig. S10.

Although purely passive electrode systems serve to demonstrate the advantages and underlying aspects of these systems, the same approaches are compatible with fully active electronics and optoelectronics. This technology allows intimate integration of finely spaced electrode systems with living tissue, enabling the kind of reliable biotic/abiotic interface with moving, biological structures that will be required for chronically implanted, high-resolution medical devices. This improved electrode/tissue interface has the potential for a positive impact on human health in many modes of use.

Methods

Thick electrode array (>25 µM) fabrication. Commercial PI films (Kapton, Dupont) with thicknesses of 25 and 75 µm were attached to a temporary carrier substrate consisting of a glass slide coated with PDMS. After cleaning the surfaces with acetone, isopropyl alcohol and deionized water, electron beam evaporation formed uniform coatings of metal (Cr/Au, 50/1450 A). Photolithography and patterned etching yielded arrays of interconnect lines. Thin layers of PI (thickness ~1.2 µm) spin-cast and patterned by reactive ion etching left only the ends of the lines exposed. Further deposition and patterning defined square metal electrode pads at these locations. Peeling these away from the PDMS-coated glass slide and bonding them to an ACF cable, using procedures described in a separate section, completed the fabrication. Supplementary Fig. S1 provides a schematic diagram and images of the process.

Thin electrode array (<10 µM) fabrication. The fabrication in this case used a carrier silicon wafer coated with a thin (~1.2 µm) spin-cast layer of PMMA (A2, MicroChem). The device substrate consisted of a film of PI (Sigma Aldrich) spin-cast onto the PMMA. Procedures similar to those described for thick devices formed the metal electrodes and PI overcoat. After fabrication, the ultrathin devices were released by dissolving the sacrificial PMMA layer. Transfer printing with a PDMS stamp delivered the devices to dry silk film substrates, coated with ~9% silk solution as an adhesive. The final step involved bonding of an ACF cable.

Mesh electrode array (<10 µM) fabrication. The first and last parts of the fabrication sequence were identical to the steps outlined in the previous section. The only difference was the addition of a step to remove certain regions of the polymer layers (that is, PI and underlying PMMA) by oxygen reactive ion etching through a mask (design in Supplementary Fig. S3) to define the mesh structure. Detailed dimensions are as follows: thickness ~2.5 µm, contact electrode size 500 µm × 500 µm, mesh width ~250 µm. (See more details in Supplementary Fig. S5.) This etching immediately followed the formation of the electrode pads.

ACF connection. The contact pads on the electrode array were first aligned with the ACF cable. Metal clips were used to apply pressure, spread evenly over the contact pad area using a piece of PDMS inserted between the ACF and the clips. Next, the clamped sample and ACF were placed in an oven preheated to ~150 °C for ~15 min. This process formed a strong mechanical bond between the electrode array and the ACF with low electrical resistance.

Data acquisition and processing. The electrode arrays were connected to a Neuralynx DigitalLynx data acquisition system through the ACF and a custom electrode interface board. The board appears in Supplementary Fig. S11. Supplementary Fig. S2 shows the connected electrode array, ACF ribbon and circuit board. The signals were sampled at the standard DigitalLynx sampling rate of 32,556 Hz per channel. The high-pass filter was set at 1 Hz and low-pass filter at 9 kHz. Custom MATLAB software (The MathWorks) was used for offline processing. Signals were down-sampled to 2,713 Hz and further low-pass filtered at 50 Hz. Responses were averaged for each stimulus and plotted per electrode.

Animal experiments. Experiments were conducted in accordance with the ethical guidelines of the National Institutes of Health and with the approval of the Institutional Animal Care and Use Committee of the University of Pennsylvania. Surgical and stimulation methods were as described in detail previously[29–31]. Briefly, adult cats (2.5–3.5 kg) were anaesthetized with intravenous thiopental with a continuous infusion (3–10 mg kg^{-1} h^{-1}) and paralysed with gallamine triethiodide (Flaxedil). Heart rate, blood pressure, end-tidal CO_2 and electroencephalograph were monitored throughout the experiment to assure depth and stability of anaesthesia and rectal temperature was kept at 37–38 °C with a heating pad. The

surface of the visual cortex was exposed with a craniotomy centred at Horsley Clarke posterior 4.0, lateral 2.0.

For visual stimulation, the corneas were protected with contact lenses after dilating the pupils with 1% ophthalmic atropine and retracting the nictitating membranes with phenylephrine (Neosynephrine). Spectacle lenses were chosen by the tapetal reflection technique to optimize the focus of stimuli on the retina. The position of the monitor was adjusted with an $x–y$ stage so that the area centralae were centred on the screen. Stimuli were presented on an Image Systems (Minnetonka) model M09LV monochrome monitor operating at 125 frames s^{-1} at a spatial resolution of $1,024 \times 786$ pixels and a mean luminance of 47 cd m^{-2}.

References

1. Kim, S. *et al*. Integrated wireless neural interface based on the Utah electrode array. *Biomed. Microdevices* **11,** 453–466 (2009).
2. Ryu, S. I. & Shenoy, K. V. Human cortical prostheses: Lost in translation? *Neurosurg. Focus* **27,** E5 (2009).
3. Andersen, R. A., Musallam, S. & Pesaran, B. Selecting the signals for a brain–machine interface. *Curr. Opin. Neurobiol.* **14,** 720–726 (2004).
4. Mehring, C. *et al*. Inference of hand movements from local field potentials in monkey motor cortex. *Nature Neurosci.* **6,** 1253–1254 (2003).
5. Ball, T. *et al*. Towards an implantable brain–machine interface based on epicortical field potentials. *Biomed. Tech.* **49,** 756–759 (2004).
6. Wilson, J. A., Felton, E. A., Garell, P. C., Schalk, G. & Williams, J. C. ECoG factors underlying multimodal control of a brain–computer interface. *IEEE Trans. Neural Syst. Rehabil. Eng.* **14,** 246–250 (2006).
7. Freeman, W. J., Rogers, L. J., Holmes, M. D. & Silbergeld, D. L. Spatial spectral analysis of human electrocorticograms including the alpha and gamma bands. *J. Neurosci. Methods* **95,** 111–121 (2000).
8. Kellis, S. S., House, P. A., Thomson, K. E., Brown, R. & Greger, B. Human neocortical electrical activity recorded on nonpenetrating microwire arrays: Applicability for neuroprostheses. *Neurosurg. Focus* **27,** E9 (2009).
9. Rubehn, B., Bosman, C., Oostenveld, R., Fries, P. & Stieglitz, T. A MEMS-based flexible multichannel ECoG-electrode array. *J. Neural Eng.* **6,** 036003 (2009).
10. Hollenberg, B. A., Richards, C. D., Richards, R., Bahr, D. F. & Rector, D. M. A MEMS fabricated flexible electrode array for recording surface field potentials. *J. Neurosci. Methods* **153,** 147–153 (2006).
11. Yu, Z. *et al*. Monitoring hippocampus electrical activity *in vitro* on an elastically deformable microelectrode array. *J. Neurotrauma* **26,** 1135–1145 (2009).
12. Meacham, K. W., Giuly, R. J., Guo, L., Hochman, S. & DeWeerth, S. P. A lithographically-patterned, elastic multi-electrode array for surface stimulation of the spinal cord. *Biomed. Microdev.* **10,** 259–269 (2008).
13. Lawrence, B. D., Cronin-Golomb, M., Georgakoudi, I., Kaplan, D. L. & Omenetto, F. G. Bioactive silk protein biomaterial systems for optical devices. *Biomacromolecules* **9,** 1214–1220 (2008).
14. Omenetto, F. G. & Kaplan, D. L. A new route for silk. *Nature Photon.* **2,** 641–643 (2008).
15. Jin, H-J. *et al*. Water-stable silk films with reduced β-sheet content. *Adv. Funct. Mater.* **15,** 1241–1247 (2005).
16. Lu, Q. *et al*. Water-insoluble silk films with silk I structure. *Acta Biomater.* **6,** 1380–1387 (2009).
17. Jiang, C. *et al*. Mechanical properties of robust ultrathin silk fibroin films. *Adv. Funct. Mater.* **17,** 2229–2237 (2007).
18. Sofia, S., McCarthy, M. B., Gronowicz, G. & Kaplan, D. L. Functionalized silk-based biomaterials for bone formation. *J. Biomed. Mater. Res.* **54,** 139–148 (2001).
19. Perry, H., Gopinath, A., Kaplan, D. L., Negro, L. D. & Omenetto, F. G. Nano- and micropatterning of optically transparent, mechanically robust, biocompatible silk fibroin films. *Adv. Mater.* **20,** 3070–3072 (2008).
20. Murphy, A. R., John, P. S. & Kaplan, D. L. Modification of silk fibroin using diazonium coupling chemistry and the effects on hMSC proliferation and differentiation. *Biomaterials* **29,** 2829–2838 (2008).
21. Altman, G. H. *et al*. Silk-based biomaterials. *Biomaterials* **24,** 401–416 (2003).
22. Santin, M., Motta, A., Freddi, G. & Cannas, M. *In vitro* evaluation of the inflammatory potential of the silk fibroin. *J. Biomed. Mater. Res.* **46,** 382–389 (1999).
23. Kim, D-H. *et al*. Silicon electronics on silk as a path to bioresorbable, implantable devices. *Appl. Phys. Lett.* **95,** 133701–133703 (2009).
24. Amsden, J. J. *et al*. Spectral analysis of induced colour change on periodically nanopatterned silk films. *Opt. Express* **17,** 21271–21279 (2009).
25. Parker, S. T. *et al*. Biocompatible silk printed optical waveguides. *Adv. Mater.* **21,** 2411–2415 (2009).
26. Soong, H. K. & Kenyon, K. R. Adverse reactions to virgin silk sutures in cataract surgery. *Ophthalmology* **91,** 479–483 (1984).
27. Chaudhury, M. K. & Whitesides, G. M. Direct measurement of interfacial interactions between semispherical lenses and flat sheets of poly(dimethylsiloxane) and their chemical derivatives. *Langmuir* **7,** 1013–1025 (1991).
28. Someya, T. *et al*. Conformable, flexible, large-area networks of pressure and thermal sensors with organic transistor active matrixes. *Proc. Natl Acad. Sci. USA* **102,** 12321–12325 (2005).
29. Padnick, L. B. & Linsenmeier, R. A. Properties of the flash visual evoked potential recorded in the cat primary visual cortex. *Vision Res.* **39,** 2833–2840 (1999).
30. Cardin, J. A., Palmer, L. A. & Contreras, D. Stimulus feature selectivity in excitatory and inhibitory neurons in primary visual cortex. *J. Neurosci.* **27,** 10333–10344 (2007).
31. Cardin, J. A., Palmer, L. A. & Contreras, D. Cellular mechanisms underlying stimulus-dependent gain modulation in primary visual cortex neurons *in vivo*. *Neuron* **59,** 150–160 (2008).

Author contributions

D-H.K., J.V., J.J.A., J.X., L.V., Y-S.K., D.C., D.L.K., F.G.O., Y.H, K-C.H., M.R.Z., B.L. and J.A.R. designed the experiments. D.H.K., E.S.F., J.V., J.J.A., J.X., L.V., Y-S.K., B.P. and J.A.B. carried out experiments and analysis. D-H.K., J.V., J.J.A., J.X., L.V., J.A.B., D.C., D.L.K., F.G.O., Y.H., B.L. and J.A.R. wrote the paper.

Additional information

The authors declare no competing financial interests. Supplementary information accompanies this paper on www.nature.com/naturematerials. Reprints and permissions information is available online at http://npg.nature.com/reprintsandpermissions. Correspondence and requests for materials should be addressed to B.L. or J.A.R.

Dae-Hyeong Kim[1][†], Jonathan Viventi[2][†], Jason J. Amsden[3], Jianliang Xiao[4], Leif Vigeland[5], Yun-Soung Kim[1], Justin A. Blanco[2], Bruce Panilaitis[3], Eric S. Frechette[6], Diego Contreras[5], David L. Kaplan[3], Fiorenzo G. Omenetto[3], Yonggang Huang[4], Keh-Chih Hwang[7], Mitchell R. Zakin[8], Brian Litt[2,6]* and John A. Rogers[1]*

[1]Department of Materials Science and Engineering, Beckman Institute for Advanced Science and Technology and Frederick Seitz Materials Research Laboratory, University of Illinois at Urbana-Champaign, Urbana, Illinois 61801, USA, [2]Department of Bioengineering, University of Pennsylvania, Philadelphia, Pennsylvania 19104, USA, [3]Department of Biomedical Engineering, Tufts University, Medford, Massachusetts 02155, USA, [4]Department of Mechanical Engineering and Department of Civil and Environmental Engineering, Northwestern University, Evanston, Illinois 60208, USA, [5]Department of Neuroscience, University of Pennsylvania School of Medicine, 215 Stemmler Hall, Philadelphia, Pennsylvania 19104, USA, [6]Department of Neurology, Hospital of the University of Pennsylvania, 3 West Gates, 3400 Spruce Street, Philadelphia, Pennsylvania 19104, USA, [7]AML, Department of Engineering Mechanics, Tsinghua University, Beijing 100084, China, [8]Defense Advanced Research Projects Agency, Arlington, Virginia 22203, USA. [†]These authors contributed equally to this work. *e-mail: littb@mail.med.upenn.edu; jrogers@uiuc.edu.

Dissolvable Films of Silk Fibroin for Ultrathin, Conformal Bio-Integrated Electronics

Dae-Hyeong Kim[1][⊥], Jonathan Viventi[2][⊥], Jason J. Amsden[3], Jianliang Xiao[4], Leif Vigeland[5], Yun-Soung Kim[1], Justin A. Blanco[2], Bruce Panilaitis[3], Eric S. Frechette[6], Diego Contreras[5], David L. Kaplan[3], Fiorenzo G. Omenetto[3], Yonggang Huang[4], Keh-Chih Hwang[7], Mitchell R. Zakin[8], Brian Litt[2,6]*, John A. Rogers[1]*

[1]*Department of Materials Science and Engineering, Beckman Institute for Advanced Science and Technology and Frederick Seitz Materials Research Laboratory, University of Illinois at Urbana-Champaign, Urbana, Illinois 61801 USA*

[2]*Department of Bioengineering, University of Pennsylvania, Philadelphia, PA 19104 USA*

[3]*Department of Biomedical Engineering, Tufts University, Medford, MA 02155, USA*

[4]*Department of Mechanical Engineering and Department of Civil and Environmental Engineering, Northwestern University, Evanston, IL 60208*

[5]*Department of Neuroscience, University of Pennsylvania School of Medicine, 215 Stemmler Hall, Philadelphia, PA 19104 USA*

[6]*Department of Neurology, Hospital of the University of Pennsylvania, 3 West Gates, 3400 Spruce Street, Philadelphia, PA 19104 USA*

[7]*AML, Department of Engineering Mechanics, Tsinghua University, Beijing 100084, China*

[8]*Defense Advanced Research Projects Agency, Arlington VA, USA*

[⊥]*D.-H. Kim and J. Viventi contributed equally.*

To whom correspondence should be addressed. E-mail: jrogers@uiuc.edu; littb@mail.med.upenn.edu

Supplementary Information

Silk dissolution test

By altering the secondary structure of a silk film, one can program the amount of time it takes for the film to dissolve in water. For this paper we want the film to dissolve within minutes, or within hours. No treatment was required to make the film dissolve in minutes. Creating some beta sheet structure by exposing to 70% ethanol for approximately 5 seconds increased the dissolution time to approximately 1 hour. To determine a dissolution rate, we made 51 square inch films, exposed them to ethanol for 5 seconds, put them in a room temperature water bath and measured their dry weight after a certain time in the water bath. See Fig 2c.

The bending stiffness of the thin film

The cross sectional geometry of the thin film is illustrated in Fig. S3a. There are n gold bricks (size $b_m \times h_m$, Young's modulus $E_{Au} = 78\,GPa$ and Poisson's ratio $\nu_{Au} = 0.44$) surrounded by PI (size $b \times h$, Young's modulus $E_{PI} = 2.5\,GPa$ and Poisson's ratio $\nu_{PI} = 0.34$). The distance between the neutral axis and bottom of the thin film is

$$y_0 = \frac{h}{2} \frac{1 + \dfrac{2h' + h_m}{h}\left(\dfrac{E_{Au}}{E_{PI}} - 1\right)\dfrac{nb_m h_m}{bh}}{1 + \left(\dfrac{E_{Au}}{E_{PI}} - 1\right)\dfrac{nb_m h_m}{bh}}, \qquad (S1)$$

where h' is the distance between bottoms of gold bricks and thin film. The bending stiffness of the thin film is

$$EI = E_{PI}bh\left(\frac{1}{3}h^2 - hy_0 + y_0^2\right)$$
$$+ \left(E_{Au} - E_{PI}\right)n\,_m b_m h_m\left[\frac{1}{3}h_m^2 + h_m(h' - y_0) + (h' - y_0)^2\right] \tag{S2}$$

The bending stiffness of the thin film on a silk backing substrate

The cross sectional geometry of the thin film on a silk backing substrate is illustrated in Fig. S3b. The silk backing substrate has a thickness H and Young's modulus $E_{Silk} = 2.8\,GPa$. The distance between the neutral axis and bottom of the thin film is

$$y_0 = \frac{h}{2}\frac{1 + \dfrac{2h' + h_m\left(\dfrac{E_{Au}}{E_{PI}} - 1\right)nb_m h_m}{h}\dfrac{nb_m h_m}{bh} - \dfrac{E_{silk}H^2}{E_{PI}h^2}}{1 + \left(\dfrac{E_{Au}}{E_{PI}} - 1\right)\dfrac{nb_m h_m}{bh} + \dfrac{E_{silk}H}{E_{PI}h}}. \tag{S3}$$

The bending stiffness of the thin film is

$$EI = E_{PI}bh\left(\frac{1}{3}h^2 - hy_0 + y_0^2\right) + E_{silk}bH\left(\frac{1}{3}H^2 + Hy_0 + y_0^2\right)$$
$$+ \left(E_{Au} - E_{PI}\right)n\,_m b_m h_m\left[\frac{1}{3}h_m^2 + h_m(h' - y_0) + (h' - y_0)^2\right]. \tag{S4}$$

A thin film wrapping around two overlapped cylinders

The beam theory gives the unwrapped part of thin film (above the connecting arc in the center frame of Fig. 4b) is (part of) a circle of radius r given by

$$r = \frac{d}{\sin\theta} - R. \tag{S5}$$

The bending energy in the thin film is obtained as

$$U_b = EI\frac{1}{r^2}r\theta + EI\frac{1}{R^2}(L - r\theta) = EI\frac{\theta\sin\theta}{d - R\sin\theta} + \frac{EI}{R^2}\left(L + R\theta - \frac{d\theta}{\sin\theta}\right). \tag{S6}$$

The adhesion energy is

$$U_a = -2\gamma b\left(L + R\theta - \frac{d\theta}{\sin\theta}\right). \tag{S7}$$

The total energy of the wrapped state is the summation of the above bending energy

and adhesion energy,

$$U_2 = \frac{EI}{R}\left[\frac{R\theta\sin\theta}{d-R\sin\theta} - \left(\frac{\gamma}{\gamma_c}-1\right)\left(\frac{L}{R}+\theta - \frac{d\theta}{R\sin\theta}\right)\right],$$ (S8)

where γ_c is given in Eq. (1).

γ_c' is obtained from Eq. (2) with $\theta = \theta_0$ as $\gamma_c' = \gamma_c\left\{1+(1+\lambda)R^2\big/\left[(1-\lambda)r_0^2\right]\right\}$ and $\lambda = r_0 d\big/\left\{(R+r_0)\sqrt{(R+r_0)^2-d^2}\sin^{-1}\left[d/(R+r_0)\right]\right\}$.

Mechanics model for mesh design

For the sheet design as shown in the left frame of Fig. 4d, the thin film is modeled as a plate. The central green part denotes the PI plate of radius r, tension stiffness $(Eh)_{PI} = \bar{E}_{PI}h$ and equi-biaxial bending stiffness $(EI)_{PI} = \bar{E}_{PI}(1+\nu_{PI})h^3\big/12$, where $\bar{E}_{PI} = E_{PI}\big/(1-\nu_{PI}^2)$ is the plane-strain modulus of PI. The yellow ring is the sandwiched composite of PI and Au of width w, tension stiffness $(Eh)_{composite} = \bar{E}_{PI}h + (\bar{E}_{Au}-\bar{E}_{PI})h_m$ and equi-biaxial bending stiffness

$$(EI)_{composite} = \bar{E}_{PI}(1+\nu_{PI})h\left(\frac{1}{3}h^2 - hy_1 + y_1^2\right)$$
$$+\left[\bar{E}_{Au}(1+\nu_{Au}) - \bar{E}_{PI}(1+\nu_{PI})\right]\left[\frac{1}{3}h_m^2 + h_m(h'-y_1) + (h'-y_1)^2\right]h_m \quad , \quad \text{where}$$

$$y_1 = \frac{h}{2}\frac{1+\dfrac{(2h'+h_m)h_m}{h^2}\left[\dfrac{\bar{E}_{Au}(1+\nu_{Au})}{\bar{E}_{PI}(1+\nu_{PI})}-1\right]}{1+\left[\dfrac{\bar{E}_{Au}(1+\nu_{Au})}{\bar{E}_{PI}(1+\nu_{PI})}-1\right]\dfrac{h_m}{h}}$$ is the distance between the neutral axis and

bottom of the thin film, and $\bar{E}_{Au} = E_{Au}\big/(1-\nu_{Au}^2)$ is the plane-strain modulus of Au. The total energy of the wrapped state, which is composed of the bending energy and membrane energy in the thin film and the adhesion energy between the thin film and

sphere, is given analytically as

$$U_{sheet} = \frac{\pi r^2}{R^2}(EI)_{PI} + \pi(Eh)_{PI}\int_0^r\left(1 - \frac{R}{x}\sin\frac{x}{R}\right)^2 x\,dx$$
$$+ \frac{2\pi rw}{R^2}(EI)_{composite} + \pi rw(Eh)_{composite}\left(1 - \frac{R}{r}\sin\frac{r}{R}\right)^2 - \pi r^2\gamma \qquad (S9)$$

For the thin film to wrap around the sphere, $U_{sheet} \leq 0$, which gives the required minimum adhesion energy per unit area γ_c^{sheet} in Eq. (3). The maximum circumferential membrane strain is

$$\varepsilon_m^{sheet} = -\left(1 - \frac{R}{r+w}\sin\frac{r+w}{R}\right). \qquad (S10)$$

The maximum interfacial normal (peeling) stress is obtained as

$$\sigma_{normal}^{sheet} = \frac{\overline{E}_{PI}(1+\nu_{PI})(h - h_m) + \overline{E}_{Au}(1+\nu_{Au})h_m}{R}\left(1 - \frac{R}{r+w}\sin\frac{r+w}{R}\right). \qquad (S11)$$

For the mesh design as shown in the right frame of Fig. 4d, the total energy of the wrapped state, which is also composed of the bending energy and membrane energy in the yellow composite ring and the adhesion energy between the thin film and the sphere, is given analytically as

$$U_{mesh} = \frac{2\pi rw}{R^2}(EI)_{composite} + \pi(Eh)_{composite}\frac{w^3}{12r}\left(1 - \sqrt{1 - \frac{r^2}{R^2}}\right)^2 - 2\pi rw\gamma. \qquad (S12)$$

From $U_{mesh} \leq 0$ for the thin film to wrap around the sphere, the required minimum adhesion energy per unit area γ_c^{mesh} in Eq. (4) is obtained. The maximum circumferential membrane strain is

$$\varepsilon_m^{mesh} = -\left[1 - \frac{R}{r+w}\sin\left(\frac{w}{2R} + \arcsin\frac{2r+w}{2R}\right)\right]. \qquad (S13)$$

For representative geometrical parameters used in the current study, e.g. $w = 250\ \mu m$,

r=1 mm and R=10 mm, ε_m^{mesh} =0.07%. The maximum interfacial normal (peeling) stress is obtained as

$$\sigma_{normal}^{mesh} = \frac{\bar{E}_{PI}\left(1+v_{PI}\right)\left(h-h_m\right)+\bar{E}_{Au}\left(1+v_{Au}\right)h_m}{R}\frac{w}{2r}\left(1-\sqrt{1-\frac{r^2}{R^2}}\right). \qquad (S14)$$

Figure Captions

Figure S1. Electrode array fabrication process using thick PI film (Kapton, Dupont, USA). a, attach PI film to PDMS coated glass. b, electrode array fabrication. c, ACF connection.

Figure S2. Images of electrode array after connection of ACF and circuit board. a, electrode array with thin (< 10 μm) substrate thickness. b, electrode array with thick (> 10 μm) substrate thickness.

Figure S3. Schematic diagram for analytical model and its modeling result. a, Cross section of the neural sensor, with geometrical parameters illustrated. **b**, Cross section of the neural sensor on a silk backing substrate. **c**, The bending stiffness of the neural sensor of thickness 7 μm and 2.5 μm on a silk backing substrate.

Figure S4. Time dependent bending stiffness change for 7 μm and 2.5 μm electrode array.

Figure S5. Design of mesh type electrode array.

Figure S6. Images of mesh type electrode array after dissolution of silk substrate.

a, on glass cylinder. b, on human brain model.

Figure S7. Wrapping experiments on single cylinder, whose diameter is a, 3.5cm, b, 1.3cm, c, 0.4cm and d, 0.1cm.

Figure S8. Wrapping experiments on overlapped cylinder. a, angled view. b, side view.

Figure S9. Modeling results. a, The critical adhesion energy and **b**, the normal (peeling) stress between the film and sphere surface for sheet and mesh designs. **c**, The critical adhesion energy for sheet and mesh designs. **d**, The normal (peeling) stress between the film and sphere surface for sheet and mesh designs.

Figure S10.   A histological section of a ~100 micron thick film embedded beneath the epidermis of a mouse.   The silk implant (B) is integrated well between the epidermis/dermis (A) and the hypodermis (C).   The section was taken 4 weeks after implantation and stained with hematoxylin and eosin.   The absence of any significant chronic inflammation indicates that the silk films are well tolerated over the examined time period.

Figure S11. Design of the circuit board used to connect the ACF ribbon to the Neuralynx DigitalLynx data acquisition system.
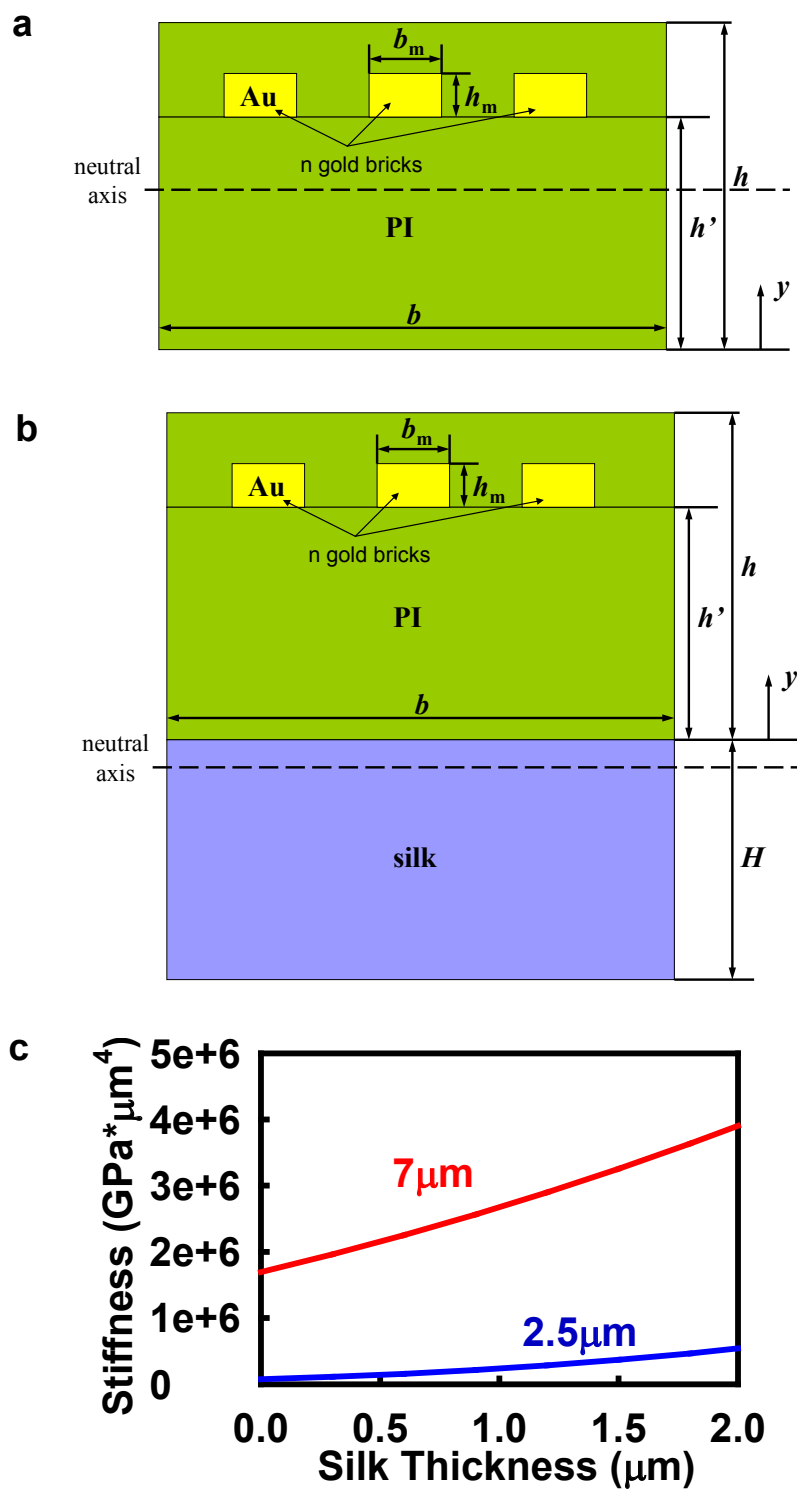
a Spin coat PDMS, attach Kapton film on glass

b Device fabrication, cut edge of kapton

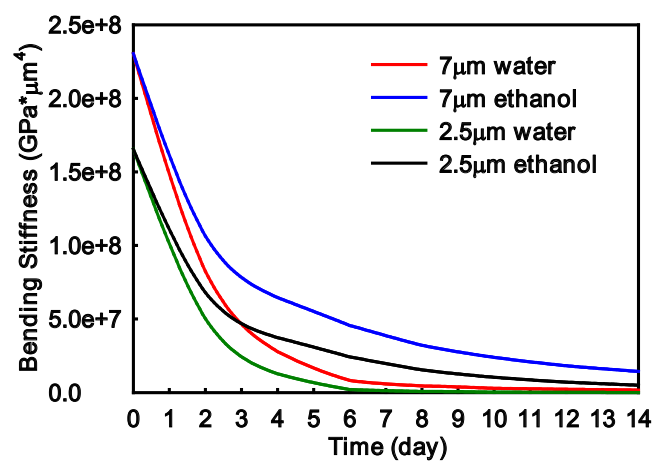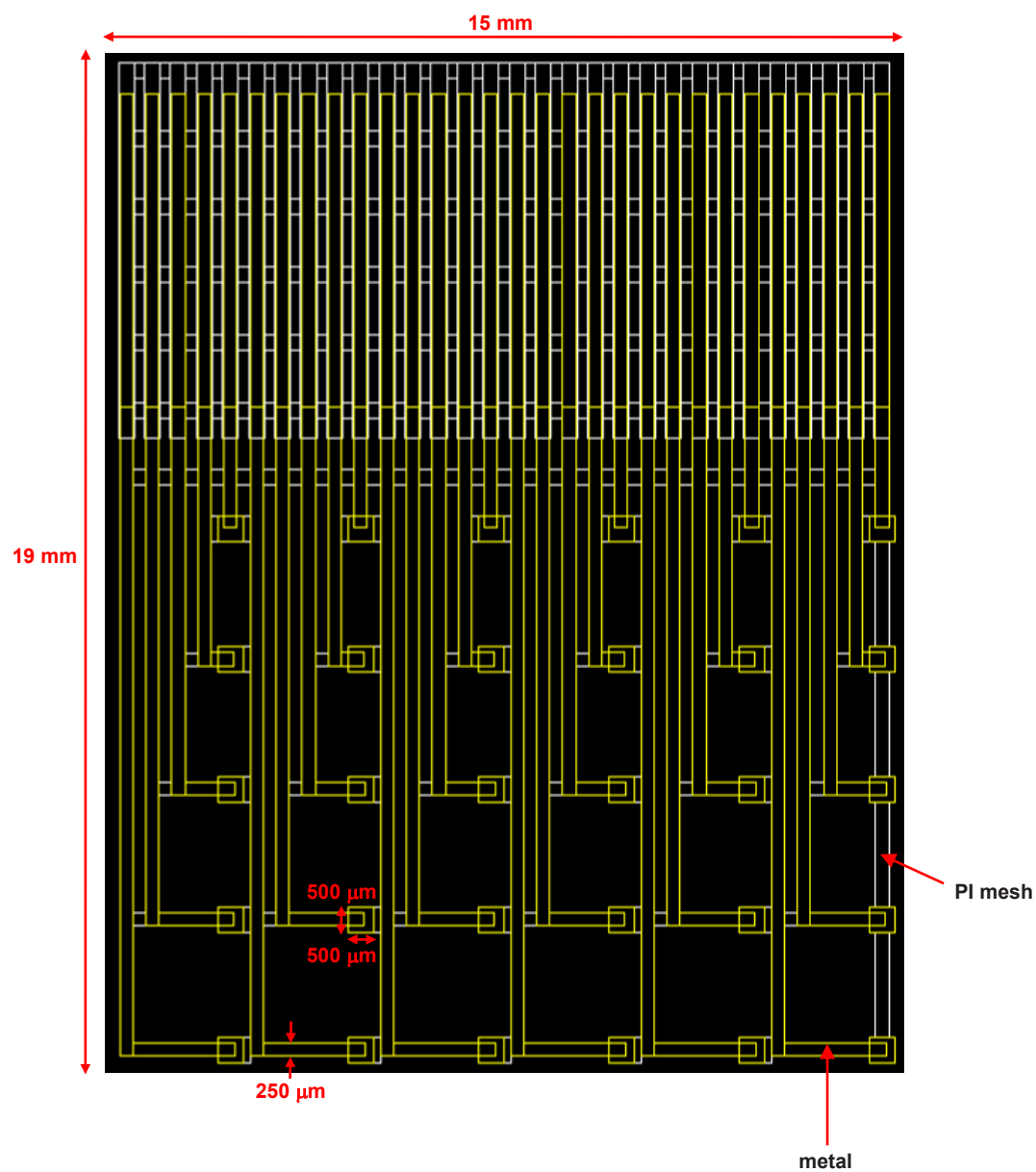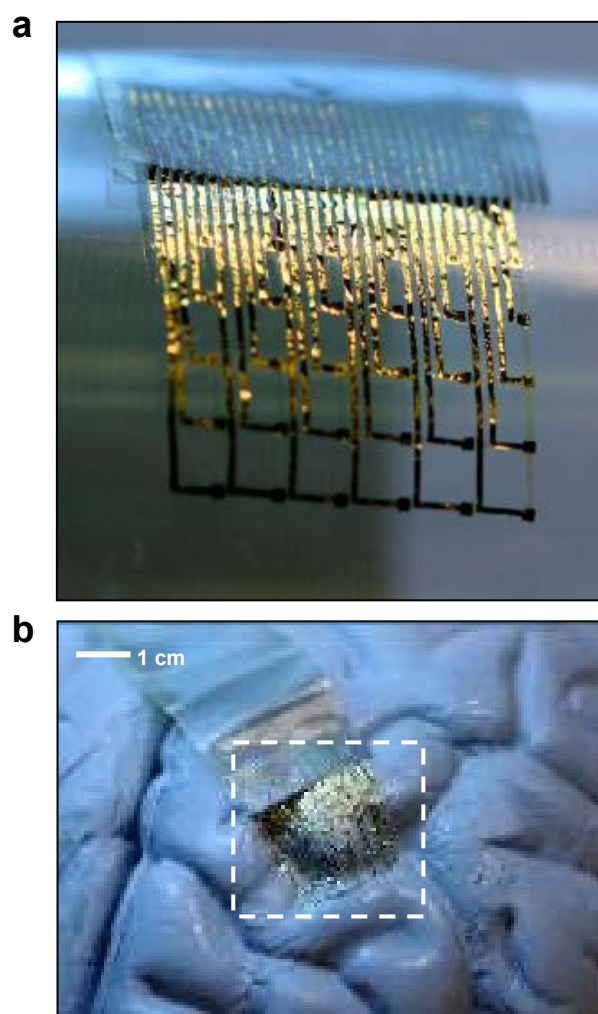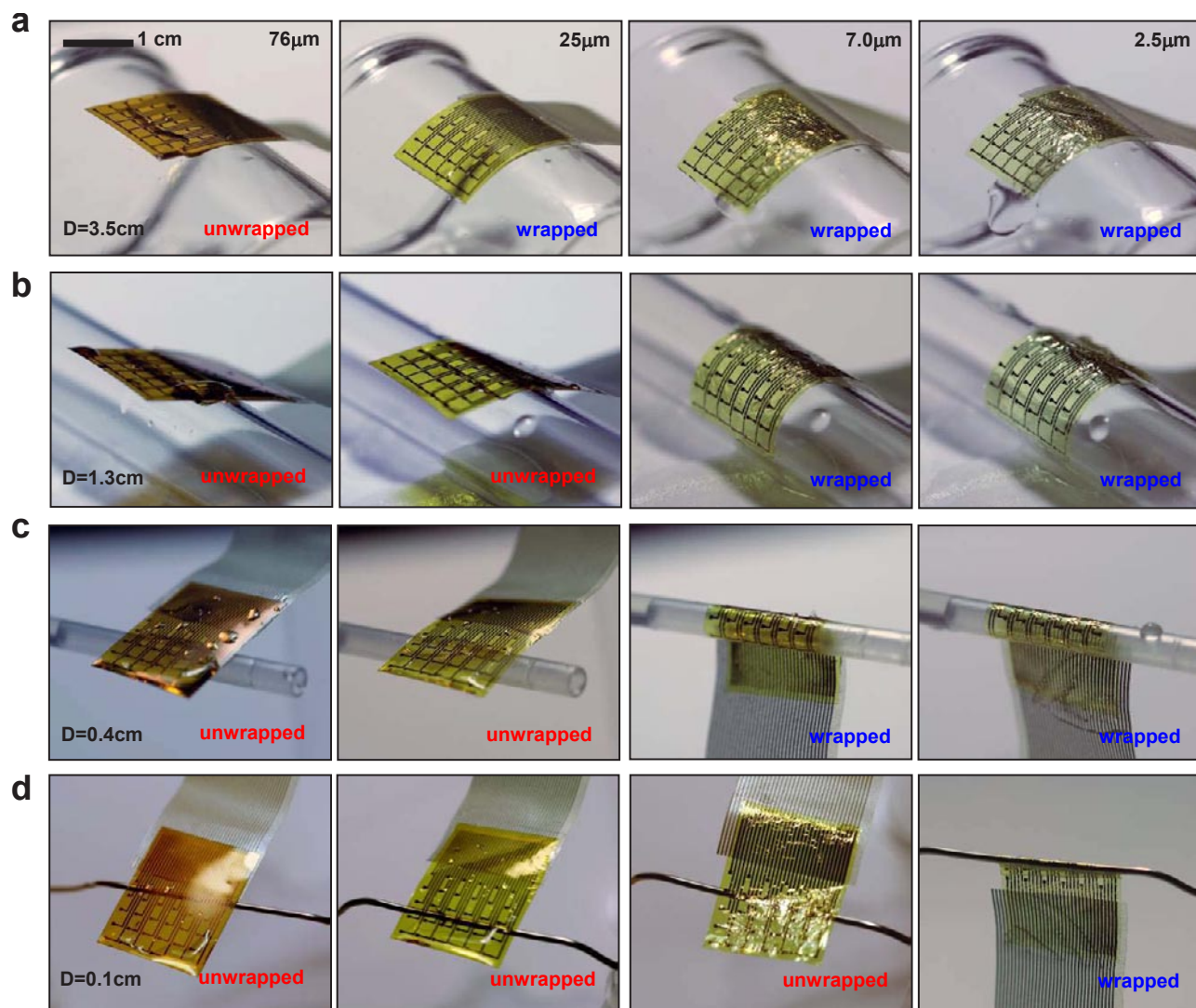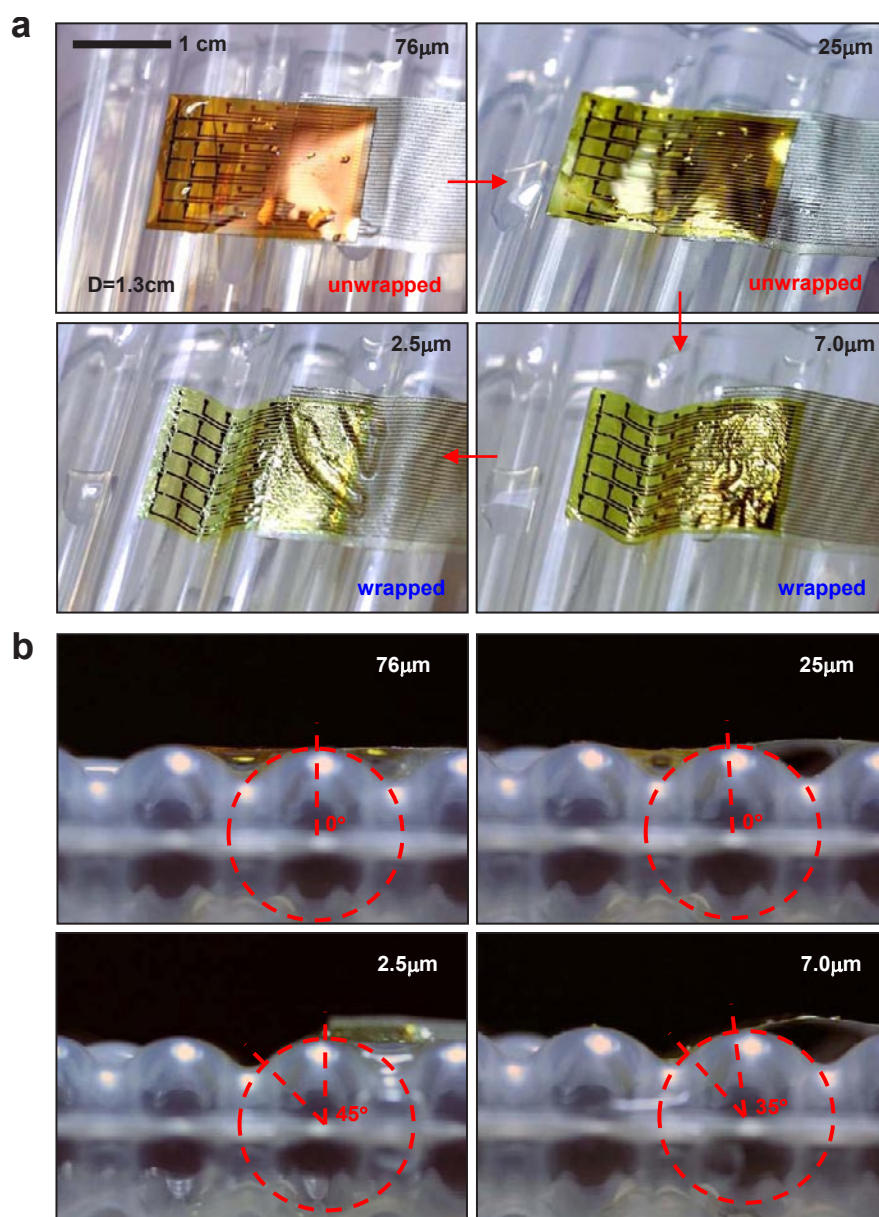c Detach from glass, connect ACF film
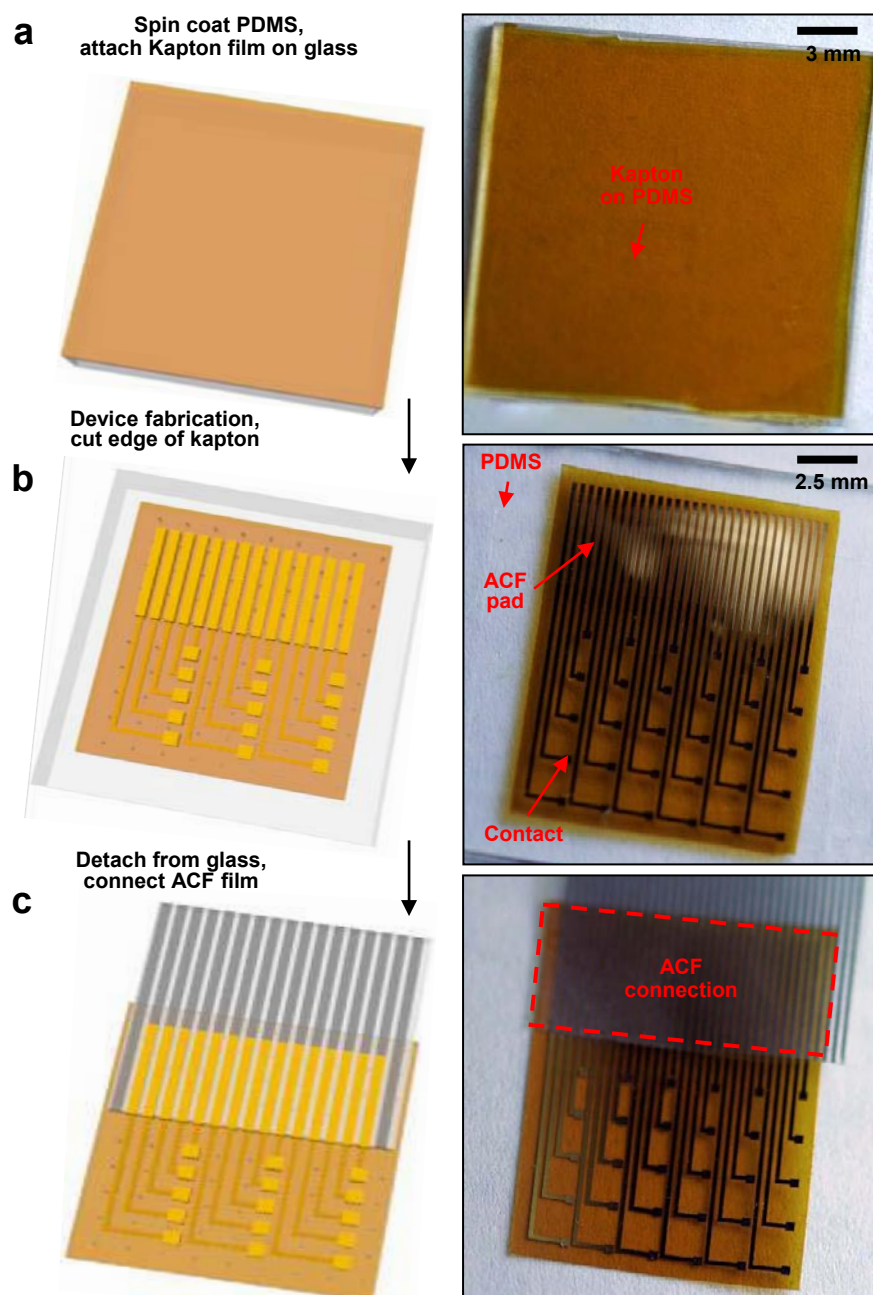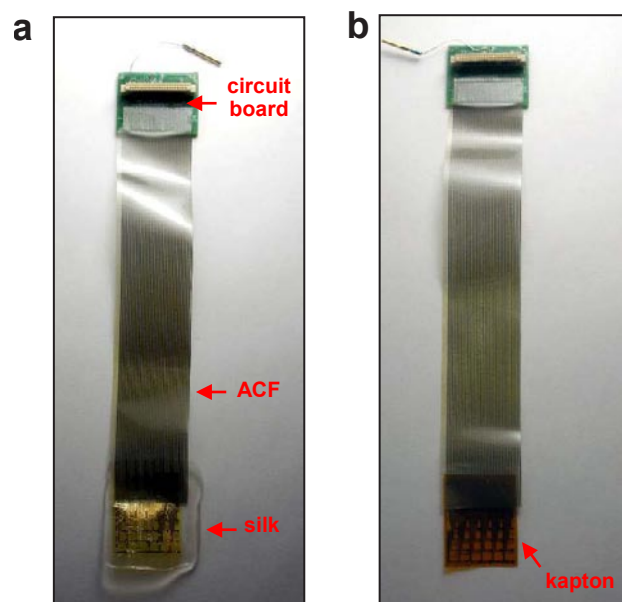
Figure S1

Figure S2

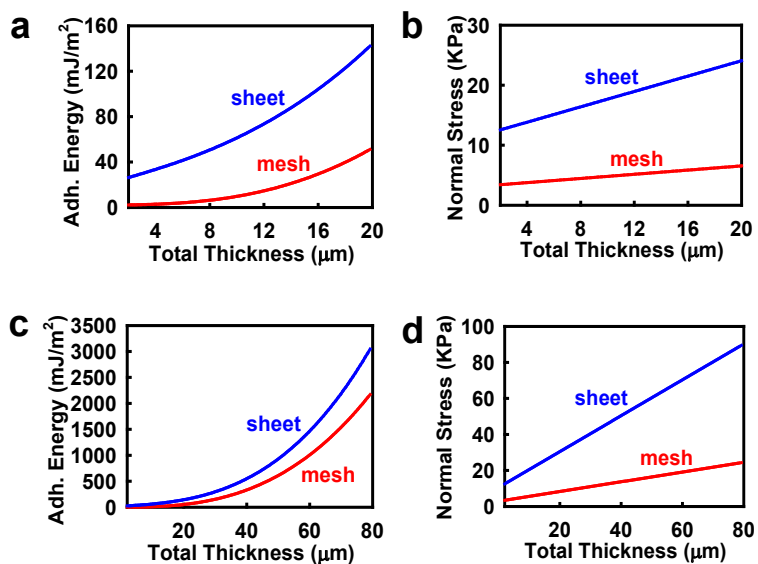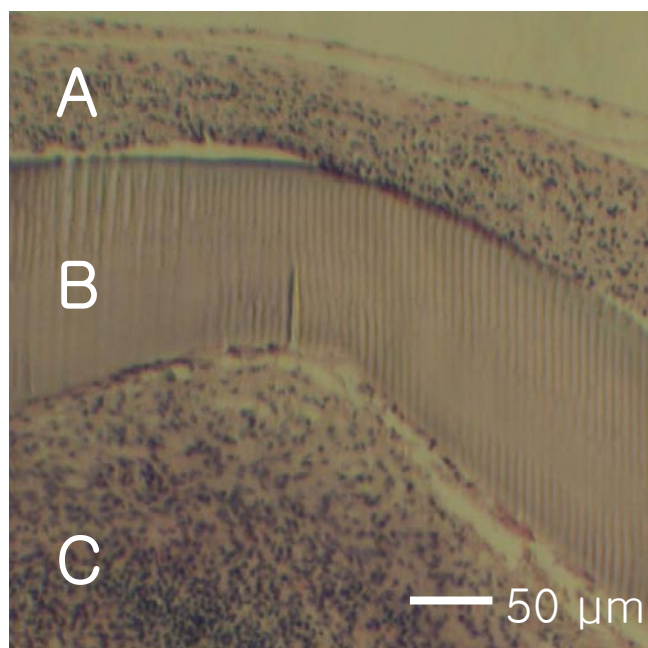Figure S3

Figure S4

Figure S5

Figure S6

Figure S7

Figure S8

Figure S9

Figure S10

Figure S11